Nanotechnology

Low-resistivity Pd nanopatterns created by a direct electron beam irradiation process free of post-treatment steps

To cite this article before publication: Alba Salvador-Porroche *et al* 2022 *Nanotechnology* in press https://doi.org/10.1088/1361-6528/ac47cf

IOP Publishing Journal Title
Journal **XX** (XXXX) XXXXXX https://doi.org/XXXX/XXXX

Low-resistivity Pd nanopatterns created by a direct electron beam irradiation process free of post-treatment steps

Alba Salvador-Porroche[1,2,3], Lucía Herrer[1,2,3], Soraya Sangiao[1,2,3], José María de Teresa[1,2,3], Pilar Cea[1,3,4] *

[1] Instituto de Nanociencia y Materiales de Aragón (INMA), CSIC-Universidad de Zaragoza,50009 Zaragoza, Spain

[2] Departamento de Física de la Materia Condensada, Facultad de Ciencias, Universidad de Zaragoza, 50009 Zaragoza, Spain

[3] Laboratorio de Microscopías avanzadas (LMA), Universidad de Zaragoza, 50018 Zaragoza, Spain

[4] Departamento de Química Física, Facultad de Ciencias, Universidad de Zaragoza, 50009 Zaragoza, Spain

*E-mail corresponding author: pilarcea@unizar.es

Abstract

The ability to create metallic patterned nanostructures with excellent control of size, shape and spatial orientation is of utmost importance in the construction of next-generation electronic and optical devices as well as in other applications such as (bio)sensors, reactive surfaces for catalysis, etc. Moreover, development of simple, rapid and low-cost fabrication processes of metallic patterned nanostructures is a challenging issue for the incorporation of such devices in real market applications. In this contribution, a direct-write method that results in highly conducting palladium-based nanopatterned structures without the need of applying subsequent curing processes is presented. Spin-coated films of palladium acetate were irradiated with an electron beam to produce palladium nanodeposits (PdNDs) with controlled size, shape and height. The use of different electron doses was investigated and its influence on the PdNDs features determined, namely: (1) thickness of the deposits, (2) atomic percentage of palladium content, (3) oxidation state of palladium in the deposit, (4) morphology of the sample and grain size of the Pd nanocrystals and (5) resistivity. It has been probed that the use of high electron doses, 30000 $\mu C \cdot cm^{-2}$ results in the lowest resistivity reported to date for PdNDs, namely 145.1 $\mu\Omega \cdot cm$, which is only one order of magnitude higher than metallic palladium. This result paves the way for development of simplified lithography processes of nanostructured deposits avoiding subsequent post-treatment steps.

Keywords: Direct-write process, electron beam, palladium acetate, low-resistance deposits

1. Introduction

Our future technology largely depends on exploiting functional properties of materials conveniently processed and patterned with precise spatial orientation as well as desired shape and size. However, such processability is particularly complicated to achieve in the case of inorganic materials, including semiconductors and metals, which are typically available in the form of crystals or powders. The academic and industrial response to these difficulties has resulted in the development of complex optical and electron-beam lithography techniques. These methodologies suffer from

several drawbacks because they are largely limited to the use of planar substrates, rely on the use of resists that may result in contaminated nanostructures as well as in undesired surface roughness from sputtered metal films. Additionally, lithographic techniques involve a multistep protocol, with long fabrication times involved, not to mention the rather expensive procedures and infrastructure required; these methodologies are also error-prone as a result of these multiple processing steps. To avoid these cumbersome procedures, direct-write approaches have emerged as maskless nanopatterning techniques with the capability of forming nanostructured materials with a variety of geometries at the nanometric scale. In this context, direct-write processes via FEBIP [1] (focused electron beam induced processing) consisting in sample exposure to an electron beam represent an advantageous methodology over multistep conventional resist lift-off lithographies, [2–6] due to the high degree of automation, precise controlled operation, nanometer-size resolution facilitated by the use of an electron beam, generation of complex 3D architectures that standard lithography cannot accomplish, and also the possibility of growing nanostructures on non-planar surface [7]. The underlying principle of focused electron beam induced methodologies is to expose a gaseous precursor material to a focused electron beam, in order to decompose this material. This results in metal-enriched permanent 2D or 3D nanostructures [8], whilst volatile fragments are pumped away. FEBIP general set up and operating principles have been comprehensively described in literature [9, 10] together with the promising applications of these deposits in the fields of nanoelectronics [11], nanomagnetics [12, 13], photonics [7], plasmonics [14, 15], superconductors [16, 17], (bio)sensors [18–20], etc. However, one of the main challenges associated to this methodology is that precursor materials do not fully dissociate under the electron beam. The final properties of the deposits are negatively determined by the low metal content, which is accompanied by the presence of carbon, oxygen and other undesired by-products that interfere with good metallic conductivity, constraining the otherwise powerful maskless synthesis paradigm of FEBIP. In order to circumvent this limitation, several post-treatment procedures have been explored to improve the metal content and remove organic impurities, including in-situ or ex-situ annealing [21–24], laser-assisted deposition and purifications [25, 26], introduction of reactive gases (e. g. O_2, H_2O, NH_3) into the chamber during irradiation [27–30], oxygen plasma cleaning, e-beam curing [31], among others [21], albeit with disadvantages such as the reduction in the nanostructure volume, morphological or compositional variations, or even changes on the electrical behavior [23, 32–35]. Furthermore, this purification extra step is not only time consuming but it also represents an additional expense for large-scale manufacturing industries.

To date, a huge variety of metalorganic precursors containing in their chemical structure Au, Ag, Pt, Pd, Ru, Fe, Co, W, Ni, Mo, Cr, etc., have been used to fabricate different types of nanopatterns, depending on the final application they were designed for [21, 36, 37]. These precursor materials can be introduced into the microscope (i) by means of a Gas Injection System (GIS) resulting in the so-called Focused Electron Beam Induced Deposition (FEBID); (ii) as a liquid (liquid-phase FEBID) that produces high-purity deposits but control of the deposit shape is problematic, (iii) but also as a pre-fabricated thin solid film (i.e. using the so-called direct-write resists which can be processed through spin-coating methods).

Nanopatterning of Pd has attracted considerable interest given its properties in catalysis [38, 39] and in hydrogen sensor applications [40, 41], as well as its relevant role in micro and nanoelectronics [42, 43]. Expressly for palladium, different gas phase precursors have been used. Good examples include palladium hexafluoroacetylacetone [$Pd(hfac)_2$] [22, 44] and (Cp)Pd(allyl) [22]. Narrowing down to resist-like or film precursors, Pd nanostructures have been fabricated by direct electron beam irradiation from palladium alkanethiolate films. For instance, in 2008 Bhuvana et al. [42], fabricated Pd nanostructures starting from a spin coated film of palladium hexadecylthiolate ($Pd(SC_{16}H_{35})_2$ using a 5 kV electron beam at 135 $\mu C \cdot cm^{-2}$. The resistivity of these direct-write nanopatterns without ex-situ treatments was ca. 1.68 $m\Omega \cdot cm$ and it was only after an extra thermolysis step at 230 ºC when a resistivity value of 30 $\mu\Omega \cdot cm$ was achieved. Lately in 2010, under similar irradiation conditions, B. Radha et al. [45] described the fabrication of Pd_4S films showing a resistivity of 16.5 $\mu\Omega \cdot cm$. The starting materials to produce patterned structures were palladium octanethiolate or palladium hexadecylthiolate spin-coated films respectively, but a post-treatment step was also applied, consisting in a thermolysis in H_2 atmosphere at 250 ºC.

The trimeric structure of palladium acetate films has been reported before as a suitable precursor for nanopatterning [46–51]. Films incorporating this organometallic compound act as a precursor allowing the direct patterning by electron beam irradiation and removal of the unexposed areas by simply rinsing the sample. The lowest resistivity values were reached by Stark et al. [48], 100 $\mu\Omega \cdot cm$ (4 kV, $1 \cdot 10^3$ $\mu C \cdot cm^{-2}$ for as-prepared spin-coated film ca. 0.1 μm thick) and Reetz et al. [47], 417 $\mu\Omega \cdot cm$ (120 kV and $2 \cdot 10^5$ $\mu C \cdot cm^{-2}$). Nonetheless, in both cases these values were obtained from nanopatterns exposed to high temperature post-treatments. Therefore, there is ongoing interest in the optimization of electron beam process conditions that permit fabrication of metallic deposits with improved properties, which in turn avoid the use of further and complex curing steps.

In this work, we extend previous research on the use of palladium acetate as an organometallic precursor by optimizing the fabrication conditions of palladium nanodeposits (PdNDs) through direct electron beam irradiation of palladium acetate spin-coated films without any subsequent post-treatment process. Figure 1 shows schematically the methodology used in this contribution to obtain PdNDs. The procedure is remarkably simple and consists of three steps: (1) preparation of the spin-coated palladium acetate films; (2) irradiation of the films with an electron beam and (3) rinse of the sample to remove the non-irradiated areas revealing the PdNDs. Importantly, by optimization of the irradiation parameters (5 kV and $30 \cdot 10^3$ $\mu C \cdot cm^{-2}$ for as-prepared spin-coated films ca. 0.12 μm in thickness) PdNDs with a resistivity of 145.1 μΩ·cm have been achieved without subsequent curing steps. This resistivity value is remarkably close to the bulk palladium resistivity at room temperature, namely 10.5 μΩ·cm [52]. As shown in the inset of Figure 1(b), the maximum resolution achievable in the growing of these PdNDs is 20 nm (80 nm considering the halo) when using an electron dose of 30000 $\mu C \cdot cm^{-2}$. Such a methodology may be relevant not only to overcome the drawbacks of post-treatment procedures, but also because avoiding heating methodologies or the use of reactive gases may open the door to a larger variety of substrates for direct-write patterning. Moreover, despite the higher dose required in this direct-write technique (compared to standard EBL using PMMA resist) the irradiation time is limited to approximately 1 minute for 100 μm^2 deposits and furthermore, the metal deposition step is avoided. Therefore, the methodology here proposed involves a much shorter time than that reported for EBL processes (in the order of hours) or direct-write electron irradiation processes followed by pros-treatment (with values in the literature in the order of at least 5 to 10 minutes). In particular, applications in the field of flexible electronics can be envisioned, due to the compatibility of flexible substrates with the three steps sketched in Figure 1 [53–55].

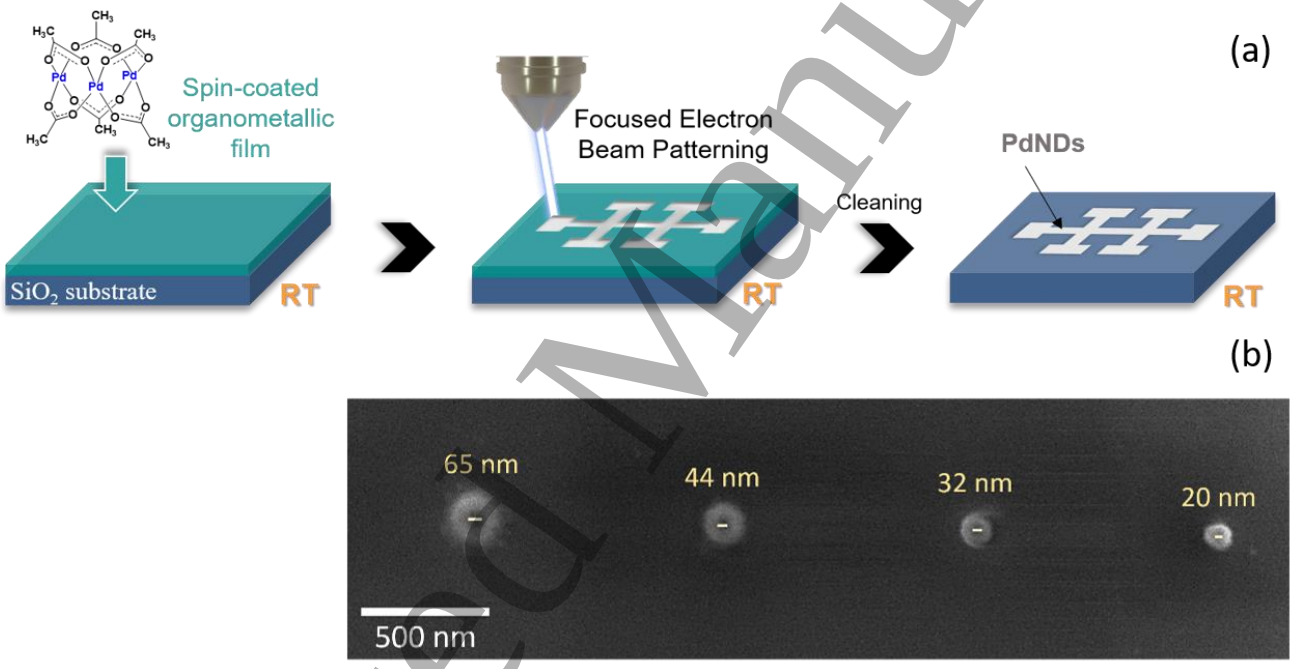

Figure 1. (a) Sketch illustrating the fabrication process of the PdNDs at room temperature (RT) designed in this contribution. The three steps are: spin-coating of the Pd organometallic film, electron-beam irradiation and removal of the unexposed organometallic film. (b) SEM micrographs of PdNDs prepared under the optimized conditions and irradiation dose of 30000 $\mu C \cdot cm^{-2}$.

2. Materials and methods

2.1 Organometallic film fabrication

Palladium (II) acetate trimer, $Pd_3(OAc)_6$, was purchased from Alfa Aesar and used as received. A fresh 0.09 M solution of $Pd_3(OAc)_6$ in $CHCl_3$ (CromAR® HPLC) was prepared and subsequently filtered through a Nylon filter (pore 0.45 μm, 13 mm diameter). Thin films of $Pd_3(OAc)_6$ were prepared onto Si/SiO_2 substrates (WS400B-6NPP/LITE from Laurell Tech.), which were cleaned by 15-minute sonication in acetone followed by 10-minute sonication in 2-propanol. A spin-coated film was obtained by spreading a volume of 10 μL of the $Pd_3(OAc)_6$ filtered solution onto a freshly cleaned Si/SiO_2 substrate. The spin-coating process include three sequential steps: (1) 10 s at 3000 rpm, as a

solvent removal step; (2) 10 s at 4000 rpm, where the solution was dynamically spread and homogeneously distributed upon the surface; and (3) 120 s at 10000 rpm for film thickness homogenization and final drying. The thicknesses of the obtained films were measured in a profilometer (KLA-Tencor P-6, Milpitas, CA, USA) performing a scratch on the sample unveiling the silicon substrate. The average thickness of the as prepared samples was 120 ± 21 nm (data obtained from 11 samples equally prepared measuring each one at 3 different scratched areas).

2.2 Palladium nanodeposits (PdNDs) fabrication and characterization

Focused Electron Beam irradiation (FEB irradiation) was performed using a Nova NanoLab 200 Dual Beam instrument from FEI Company equipped with a vertical 30 kV field-emission electron column. Patterns of ~ 1500 μm^2 were exposed using an electron beam voltage of 5 kV with doses in the 200 - 30000 $\mu C \cdot cm^{-2}$ range. After irradiation, samples were developed in $CHCl_3$ for 30 s to dissolve the unexposed areas, whilst the irradiated regions remained on the substrate.

Current versus voltage (*I-V*) curves were obtained by using a four-probe Kleindiek Nanotechnik system with electrical microprobes placed inside a Helios NanoLab 650 Dual Beam instrument from FEI Company. These measurements were done by injecting a DC current through the two outer microprobes by means of a 6221 DC current source while a 2182A nanovoltmeter was used to measure the voltage drop across the two inner microprobes. Keithley devices are connected to the microprobes via a chamber feedthrough.

Compositional analysis of the PdNDs was carried out by energy-dispersive X-ray spectroscopy (EDS) in an Inspect F-50 Scanning Electron Microscope (SEM) from FEI Company equipped with an INCA 350 detector. These experiments were performed in ~ 96 μm^2 areas and using an accelerating voltage of 5 kV.

Particle-size characterization and cross-sectional images were performed from selected deposits by Transmission Electron Microscopy (TEM) and Scanning Transmission Electron Microscopy (STEM), respectively in a Tecnai F30 Microscope from FEI Company, operating at 300 kV. For that, lamellae were prepared (PdNDs had been previously protected with Pt-FEBID and Pt-FIBID) onto Cu TEM grids.

PdNDs deposits and pristine films were characterized by X-ray photoelectron spectroscopy (XPS) in a Kratos AXIS ultraDLD spectrophotometer including a monochromatic Al Kα X-ray source (1486.6 eV) with a pass energy of 20 eV. The treatment of the spectra and further analysis were performed by the CasaXPS v.2.3.15 software, where the binding energies have been referenced to the C1s peak at 284.9 eV. Peak fitting was done by using standard line shape GL(30), except for the asymmetric signal associated to metallic palladium for which the line shape LA(1.9, 7, 2) was applied.

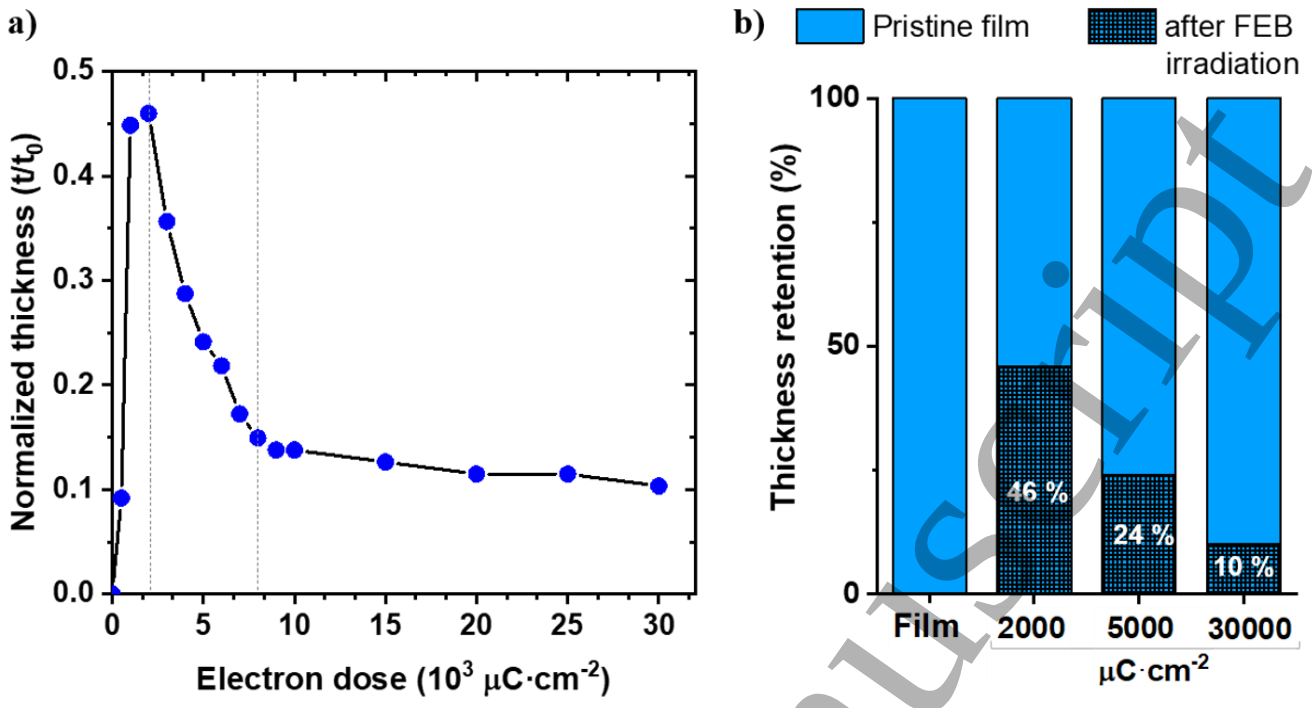

Figure 2. (a) Normalized PdNDs thicknesses of exposed areas after development. Data are normalized with respect to the as-prepared film thickness. (b) % thickness retention relative to the pristine film thickness.

PdNDs thicknesses after FEB irradiation and $CHCl_3$ washing step were determined employing the above mentioned profilometer and also by using a Multimode 8 AFM microscope from Bruker operating in ambient air conditions and tapping mode. RTESPA-300 cantilevers (resonance frequency ≈ 300 kHz, force constant ≈ 40 N·m^{-1}, nominal values, ≈ 8 nm radius), purchased from Bruker were used. The final thickness of the PdNDs represents a 10–50% of the initial film thickness, with this percentage depending on the applied electron dose as shown in section 3.

3. Results and discussions

Patterned samples were prepared by a maskless, direct-write fabrication methodology consisting of three simple subsequent steps as indicated in Figure 1(a) and capable of defining metal deposits at the nanometer scale. Several parameters upon the beam irradiation process have been modified to determine how such parameters may influence the electrical properties of the patterned films. These studies are presented in the following sub-sections.

3.1 FEB irradiation on a $Pd_3(OAc)_6$ film for PdNDs fabrication.

$Pd_3(OAc)_6$ films (see the chemical structure of the palladium acetate in Figure 1) were decomposed by FEB irradiation in ca. 1500 µm^2 areas using different electron doses (200, 300, 400, 500, 1000, 2000, 3000, 4000, 5000, 6000, 7000, 8000, 9000, 10000, 15000, 20000, 25000 and 30000 µC·cm^{-2}, Figure 2(a)). The optimized electron beam parameters were 5 kV of accelerating voltage, 400 pA of current and 1 µs of dwell time. Given that the PdNDs were fabricated using as-prepared spin-coated films with different thicknesses (in the 90-140 nm range), the PdNDs thickness is presented here in terms of normalized thickness, which is defined as the PdNDs thickness divided by the as-prepared spin-coated film thickness. The PdNDs normalized thickness was found to be dependent on the applied electron dose, Figure 2(a). Note that in Figure 2(a) all the thicknesses reported are for films after irradiation and development. In films where the applied electron dose was lower than 500 µC·cm^{-2} the irradiated areas were removed during the development step (zero thickness), due to an insufficient electron dose to decompose and change the solubility of the $Pd_3(OAc)_6$ film. In contrast,

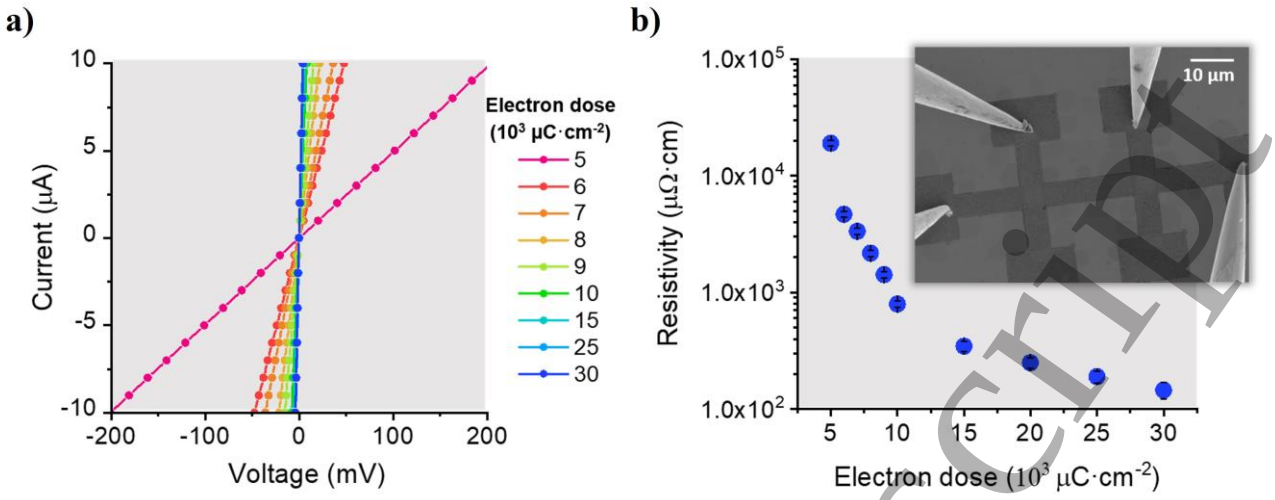

Figure 3. (a) *I-V* curves showing the linear dependence for electron doses from 5000 to 30000 μC·cm^{-2}. (b) Measured resistivity as a function of the applied electron dose.

film areas exposed to higher doses (> 500 μC·cm^{-2}) were sufficiently decomposed to become insoluble in the developing agent and therefore, they remained as PdNDs on the Si/SiO_2 surface after the washing step. For doses larger than the critical 500 μC·cm^{-2} value but below 2000 μC·cm^{-2}, the predominant mechanism is the decomposition of the organometallic film and subsequent decrease in the film solubility, i.e., an increase in the film thickness after irradiation is observed, Figure 2(a). Irradiations above 2000 μC·cm^{-2} result in a decrease in the film thickness due to elimination of volatile compounds accompanied by a densification of the film. Figure 2(b) illustrates the film thickness evolution upon increasing the applied dose for a 90 nm-thick sample. For instance, a dose of 2000 μC·cm^{-2} results in a 54% thickness reduction, whilst a higher dose of 30000 μC·cm^{-2}, leads to a thickness reduction of ca. 90%, yielding deposits with a thickness of ca. 10 nm. Figure 2(b) depictures the percentage of retention of the film thickness with the applied electron dose, where a drastic decrease in the thickness of the films is observed between 2000 and 8000 μC·cm^{-2}, after which the thickness of the film decreases much more slowly with increasing irradiation doses.

3.2. Four-probe technique for electrical measurements

Current versus voltage (*I-V*) curves were recorded by using a four-probe technique at room temperature from which the electrical resistivity of the PdNDs was obtained. These electrical measurements were performed for deposits fabricated with electron doses ranging from 500 up to 30000 μC·cm^{-2}, Figure 3(a). Deposits fabricated with electron doses lower than 5000 μC·cm^{-2} do not exhibit a linear *I-V* dependence (data not shown in Figure 3(a) for clarifying purposes). In contrast, those grown under electron doses higher or equal to 5000 μC·cm^{-2} show a linear *I-V* dependence, Figure 3(a), as expected for an ohmic behaviour. The electrical resistance was obtained from the linear fits in the *I-V* plot. By combining the electrical resistance together with the thickness, the width and length of the PdND, the electrical resistivity was determined and represented as a function of the electron dose, Figure 3(b). The electrical resistivity of the PdNDs is considerably reduced upon increasing the electron dose. Resistivity values lower than 1000 μΩ·cm are achieved for doses higher than 9000 μC·cm^{-2}. Remarkably, values as low as 145 μΩ·cm, (only one order of magnitude higher than bulk metallic palladium, 10.5 μΩ·cm) were obtained for PdNDs fabricated by applying an electron dose of 30000 μC·cm^{-2}.

The analysis of the electrical properties here shown reveals that samples irradiated with an electron dose in the 500-4000 μC·cm^{-2} range have a rather low conductance and a non-linear behaviour albeit these irradiation doses are enough to turn the irradiated palladium acetate insoluble in the developing organic solvent. Such a result could open the way to the fabrication of patterned surfaces composed of insulating and conducting nearby regions by just applying different electron doses to the selected areas of the sample.

3.3. Compositional analysis by EDS

In order to determine whether there is a correlation between the electrical resistivity of the measured PdNDs and their atomic content, a semiquantitative compositional analysis was performed by using energy-dispersive X-ray spectroscopy (EDS) in areas of ~ 96 μm^2, Figure 4(b). The atomic percentages of Pd, C and O for the irradiated samples in the range from 500 to 30000 $\mu C \cdot cm^{-2}$ are represented in Figure 4(a). This plot shows an increase in the Pd% atomic content as the electron dose rises up to 5000 $\mu C \cdot cm^{-2}$. Higher doses do not result in a further increase of the global Pd% atomic content, which remains practically constant with a value of ca. 40 ± 5% at. As indicated above, the non-linear behaviour in *I-V* plots is observed for electron doses lower than 4000 $\mu C \cdot cm^{-2}$, which accordingly to Figure 4 corresponds to deposits where the Pd% atomic content is lower than 32%. On the other hand, the fill factor calculated from Figure 4(b) - employing the ImageJ 1.53 k V 1.8.0_172 program -is 77.3%. One of the main disadvantages of pinholes could be a very high electrical resistivity but in this case, this has been ruled out due to the values around 145 μΩ cm obtained for the highest doses.

3.4. Palladium oxidation state study by XPS

Figure 4(a) shows the % atomic content of Pd, but the EDS analysis does not provide any information about the oxidation state of Pd. This fact together with the observation of a drastic decrease in the electrical resistivity of PdNDs as the electron dose is increased above 5000 $\mu C \cdot cm^{-2}$, Figure 3(b) - despite these deposits exhibit a similar Pd% atomic content - prompted us to obtain additional information

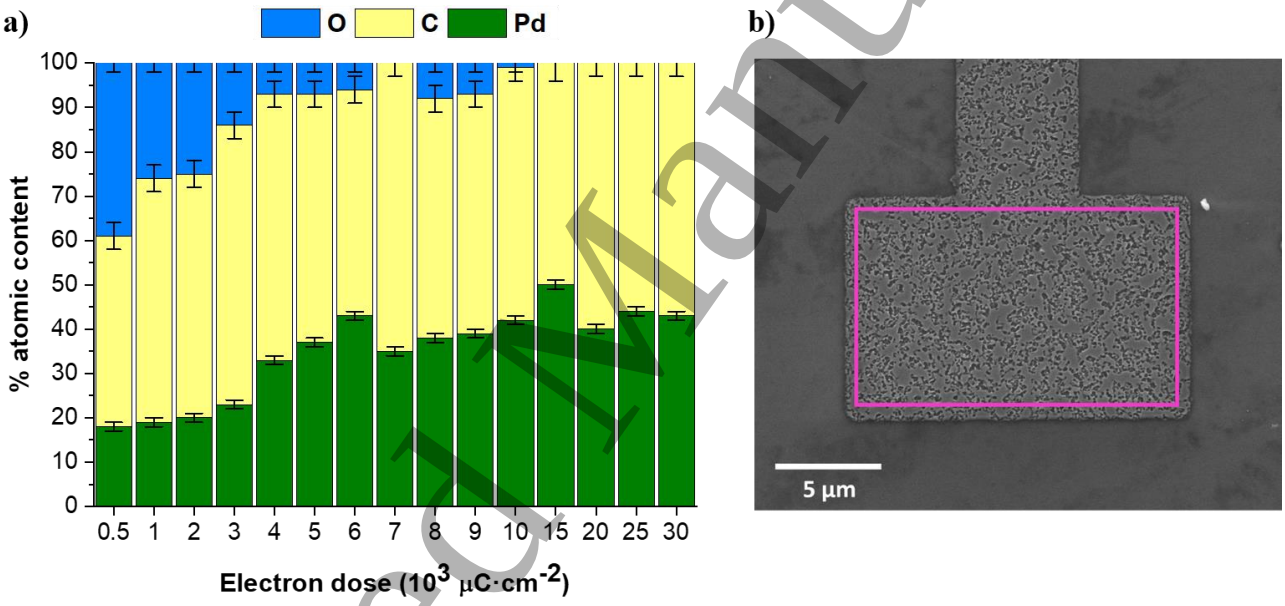

Figure 4*. (a) Atomic percentages of palladium, carbon and oxygen in PdNDs irradiated with electron doses in the 500 to 30000 $\mu C \cdot cm^{-2}$ range. (b) SEM micrograph of a PdND fabricated at 30000 $\mu C \cdot cm^{-2}$. EDS studied area marked in pink.*

through an X-ray Photoelectron Spectroscopy (XPS) analysis of the PdNDs. The decrease of electrical resistivity with the electron dose could be explained by an increase in the presence of metallic palladium, Pd^0. Thus, XPS is used here to identify the chemical oxidation state of the palladium present in the sample. For simplifying and comparison purposes, the data results presented henceforward will refer to PdNDs fabricated by applying doses of 5000 and 30000 $\mu C \cdot cm^{-2}$. Figure 5(a) shows the XPS Pd 3d region spectra for: (I) the powder compound $Pd_3(OAc)_6$; (II) the as-prepared spin-coated film; and (III and IV) two PdNDs (areas of 110 μm^2) fabricated under electron doses of 5000 and 30000 $\mu C \cdot cm^{-2}$, respectively. Concerning the spectra of the $Pd_3(OAc)_6$ powder and as-prepared film, there is a main peak at 338.5 eV (spectrum I) and 338.4 eV (spectrum I) attributed to Pd^{2+} $3d_{5/2}$ [56–59]. In both cases a small contribution (~6-7% area) of PdO/PdO_x $3d_{5/2}$ appears at 336.8, which is attributed here to the presence of palladium oxides in the powder compound. Importantly, a comparison of spectrum I

and II shows no meaningful variations between the powder and the as prepared spin-coated film. This result indicates that the palladium oxidation state is not affected upon the spin-coating film fabrication process. In contrast, the XPS spectra of the PdNDs changes dramatically upon irradiation. PdNDs fabricated using an electron dose of 5000 μC·cm^{-2}, Figures 5.(a.III) and 5(b), show a reduction in the Pd^{2+}% content from 88% in the as prepared spin-coated film to 51.5% after irradiation. This phenomenon is accompanied by a subsequent increase in the content of palladium oxides, carbides and small clusters formed on account of decomposition of the starting organometallic compound [60], peaks at 337.2 ($3d_{5/2}$) and 342.3 eV ($3d_{3/2}$). This result together with the *I-V* curve for PdNDs obtained by applying an electron dose of 5000 μC·cm^{-2} (Figure 3.a) suggest that these FEB irradiation conditions to the as-prepared spin-coated film results in stable PdNDs exhibiting a non-metallic conduction [61]. In contrast, when a dose of 30000 μC·cm^{-2} is used for the PdNDs fabrication, Figure 5(a.IV), the electron irradiation results in reduction of Pd^{2+} to Pd^0. In this case, the quantification of the peaks at 335.9 eV ($3d_{5/2}$) and 341.2 eV ($3d_{3/2}$) indicates that 64.5% of palladium in the sample is Pd^0, whilst the peaks at 338.2 and 343.3 eV, correspond to the $3d_{5/2}$ and $3d_{3/2}$ of remaining Pd^{2+}, respectively. In conclusion, the XPS study here presented indicates that irradiation of the as-prepared spin-coated films with the highest electron dose (30000 μC·cm^{-2}) results in reduction of Pd^{2+} into Pd^0, i.e., metallic palladium, explaining why the measured resistivity is two orders of magnitude lower compared to the 5000 μC·cm^{-2} electron dose, Figure 5(b) and Figure 3(b). A similar increase in the Pd^0 proportion was previously observed by XPS, but only after annealing the sample at high temperatures [62]. Thus, by using the fabrication methodology here presented it is possible to directly obtain PdNDs in which more than the

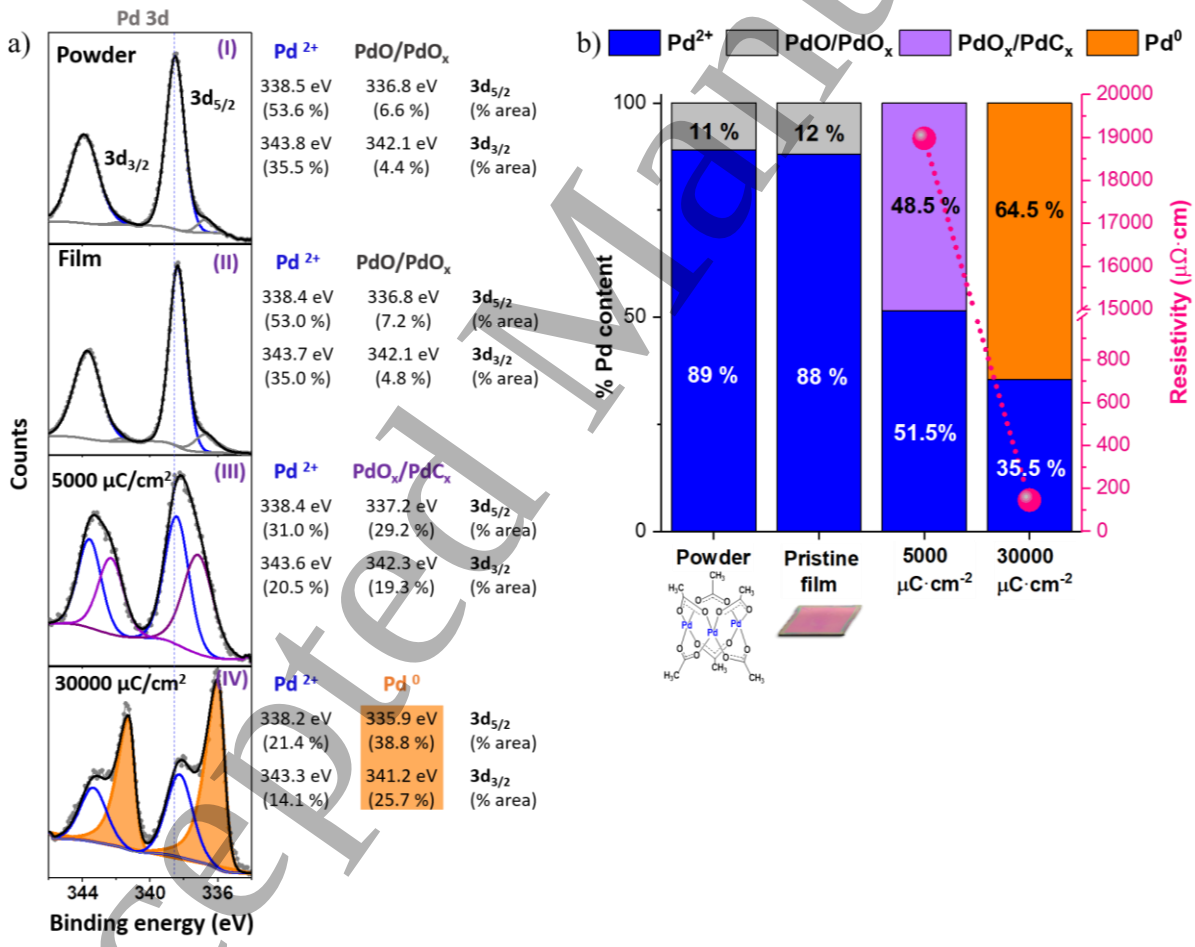

Figure 5. (a) XPS spectra for the indicated samples recorded for the Pd 3d and the correspondent peak deconvolution. (b) Left Y axis: % Pd content based on the % area corresponding the Pd 3d5/2 peak for each chemical Pd oxidation state at each sample. Right Y axis: measured resistivity for PdNDs prepared using electron doses of 5000 and 30000 μC·cm^{-2}.

64% of the palladium is metallic palladium, which in addition exhibits a rather low resistivity without the further need of a thermal post-treatment or other additional steps.

3.5. Structural and compositional analysis of PdNDs by TEM

Additional experiments in a Tecnai F30 microscope were carried out in PdNDs grown with electron doses of 5000 and 30000 μC·cm^{-2} to better understand their difference in electrical resistivity. For that, cross-sectional lamellae of the selected samples deposited onto Si/SiO_2 substrates were prepared and subsequently attached to TEM Cu grids for their analysis. On the other hand, size and morphological information was investigated in TEM mode operating at 300 kV. TEM micrographs, shown in Figure 6(a) and 6(b), reveal that particle size increases with increasing electron dose. This larger particle size is attributed to particle agglomeration, which facilitates the passage of the electrical current from some particles to others leading to a lower electrical resistivity. Particle agglomeration is tentatively attributed here to annealing effects at high electron doses since elevated temperatures favour the migration of atoms, which results in formation of larger grains and an increase in the crystalline quality of the films [63, 64]. Similarly, previous work on Pt deposits grown by FEBID has shown that post-growth electron irradiation produces an increase in the grain size and a decrease in the electrical resistivity [65]. Additionally, High-Angle Annular Dark Field (HAADF) images were obtained in STEM mode operating at 300 kV. HAADF images, shown in Figures 6(c) and 6(d), indicate

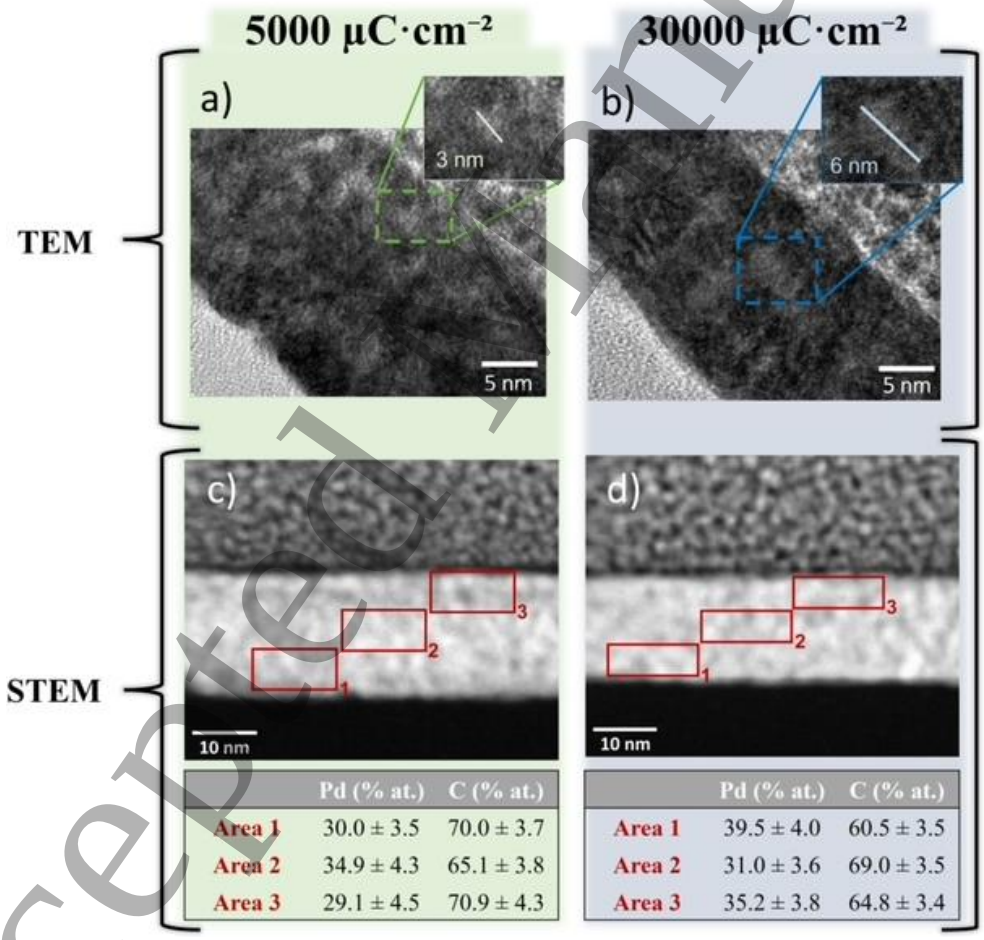

	Pd (% at.)	C (% at.)
Area 1	30.0 ± 3.5	70.0 ± 3.7
Area 2	34.9 ± 4.3	65.1 ± 3.8
Area 3	29.1 ± 4.5	70.9 ± 4.3

	Pd (% at.)	C (% at.)
Area 1	39.5 ± 4.0	60.5 ± 3.5
Area 2	31.0 ± 3.6	69.0 ± 3.5
Area 3	35.2 ± 3.8	64.8 ± 3.4

Figure 6. (a, b) Some particle size measurements in TEM micrographs of PdNDs grown with an electron dose of 5000 and 30000 μC·cm^{-2}, respectively. (c, d) HAADF-STEM images of PdNDs grown with an electron dose of 5000 and 30000 μC·cm^{-2}, respectively. EDS results carried out in three different areas are also presented (red boxes).

that PdNDs exhibit a homogeneous thickness and low roughness. On the other hand, the atomic composition was investigated by EDS in STEM mode in three selected areas from bottom to top, as indicated in red squares in Figures 6(c) and (d). As indicated in the inset table in Figure 6, the palladium content remains roughly constant with values of 31% for 5000 $\mu C \cdot cm^{-2}$ and 35% for 30000 $\mu C \cdot cm^{-2}$, which is in excellent agreement with the EDS results obtained in the SEM (section 3.3). If one combines the results shown above, it can be concluded that the electron beam, which is primarily utilized for decomposition of the palladium acetate and subsequent PdNDs deposition, plays an additional role in the growth process: high electron doses also result in a curing process of the PdNDs promoting the reduction of oxidized palladium to metallic palladium. This curing process may be attributed to two effects. On the one hand, a thermal annealing of the sample – induced by the energy provided by high electron doses – which may result in additional cracking of precursor molecules [31]. On the other hand, the electron beam may lead to a direct electron-stimulated reduction of the higher oxidation states of palladium to Pd^0 with subsequent oxidation of carbonaceous species [34, 66, 67]. These phenomena are accompanied by a densification of the sample (decrease in the thickness of the deposits) as well as agglomeration of palladium particles, with the subsequent decrease in the resistivity of the sample as compared to PdNDs fabricated at low electron doses.

4. Conclusions

Needless to say, the most convenient process for generation of patterned metal nanodeposits would consist in a single-step process. Here, we have presented a direct-write maskless technique consisting in the electron beam irradiation of a palladium acetate spin-coated film, which results in enriched metallic Pd nanostructures with low resistivity values that do not require subsequent curing processes. In particular, systematic experimental parameters were investigated to demonstrate the potential of using high electron doses to obtain PdNDs exhibiting a low resistivity, only one order of magnitude higher than pure bulk palladium. In addition, this direct-write protocol has been proven to be reproducible, simple, and effective. The working mechanism of the direct patterning process is tentatively ascribed to the local heating due to the electron beam interaction with matter together with the electron-induced reduction of Pd^{2+} to Pd^0. Importantly, despite the post-growth annealing of deposits fabricated with electron beam irradiations has been widely used in the literature for tuning the metal content of the patterned samples, the methodology here presented, with the application of high electron doses, has been proven as an efficient tool to avoid multiple processing steps. Moreover, the combined application of low and high electron doses to different areas in the as-prepared spin-coated films allows the fabrication of patterned structures with well-defined insulating and conducting domains. In summary, the low thickness value, homogeneity, and the highly defined profile achieved for these nanodeposits together with their low resistivity empower the use of this direct-write technology for its use in nanoelectronics, molecular electronics, and other applications including the construction of arrays of nanoelectrodes, nanopatterned catalytic surfaces, etc. Currently, we are exploring specific applications of this methodology in the field of nanoelectronics (e.g. contact and determination of electrical properties of nanowires).

Acknowledgements

This research was supported by the Spanish Ministry of Science through the grant numbers PID2019-105881RB-I00, MAT2017-82970-C2-2-R and PID2020-112914RB-I00, including FEDER funding, from CSIC through projects PIE202060E187 and Research Platform PTI-001, and by Gobierno de Aragón through the grant numbers LMP33-18 and E31_20R with European Social Funds (Construyendo Europa desde Aragón). The following networking projects are acknowledged: Spanish Nanolito (MAT2018-102627-T) COST-FIT4NANO (action CA19140) and OsMolsys (RED2018-102833-T). We acknowledge technical support by the LMA technicians at Universidad de Zaragoza..

References

[1] Fedorov AG, Kim S, Henry M, et al. 2014. Focused-electron-beam-induced processing (FEBIP) for emerging applications in carbon nanoelectronics. *Appl Phys A*; **117**: 1659–1674.

[2] Wang W, Pfeiffer P, Schmidt-Mende L. 2020. Direct Patterning of Metal Chalcogenide Semiconductor Materials. *Adv Funct Mater*; **30**: 2002685.

[3] Bi K, Chen Y, Wan Q, et al. 2019. Direct electron-beam patterning of transferrable plasmonic gold nanoparticles using a HAuCl4 /PVP composite resist. *Nanoscale*; **11**: 1245–1252.

[4] Prima G Di, Sachser R, Trompenaars P, et al. 2019. Direct-write single electron transistors by focused electron beam induced deposition. *Nano Futur*; **3**: 025001.

[5] Taal AJ, Rabinowitz J, Shepard KL. 2021. mr-EBL: ultra-high sensitivity negative-tone electron beam resist for highly selective silicon etching and large-scale direct patterning of permanent structures. *Nanotechnology*; **32**: 245302.

[6] Fernández-Pacheco A, Skoric L, De Teresa JM, et al. 2020. Writing 3D nanomagnets using focused electron beams. *Materials (Basel)*; **13**: 3774.

[7] Pakeltis G, Hu Z, Nixon AG, et al. 2019. Focused

Electron Beam Induced Deposition Synthesis of 3D Photonic and Magnetic Nanoresonators. *ACS Appl Nano Mater*; **2**: 8075–8082.

[8] Huth M, Porrati F, Dobrovolskiy O V. 2018. Focused electron beam induced deposition meets materials science. *Microelectron Eng*; **185**–**186**: 9–28.

[9] Clericò V, Amado M, Diez E. 2020. Electron beam lithography and its use on 2D materials. In: *Nanofabrication*. IOP Publishing. Epub ahead of print December 2020. DOI: 10.1088/978-0-7503-2608-7ch3.

[10] Pablo-Navarro J, Sangiao S, Magén C, et al. 2020. Focused electron beam induced deposition. In: *Nanofabrication*. IOP Publishing. Epub ahead of print December 2020. DOI: 10.1088/978-0-7503-2608-7ch4.

[11] George HC, Orlova TA, Orlov AO, et al. 2011. Novel method for fabrication of nanoscale single-electron transistors: Electron beam induced deposition of Pt and atomic layer deposition of tunnel barriers. *J Vac Sci Technol B, Nanotechnol Microelectron Mater Process Meas Phenom*; **29**: 06FB01.

[12] Keller L, Al Mamoori MKI, Pieper J, et al. 2018. Direct-write of free-form building blocks for artificial magnetic 3D lattices. *Sci Rep*; **8**: 6160.

[13] Pablo-Navarro J, Sanz-Hernández D, Magén C, et al. 2017. Tuning shape, composition and magnetization of 3D cobalt nanowires grown by focused electron beam induced deposition (FEBID). *J Phys D Appl Phys*; **50**: 18LT01.

[14] Höflich K, Yang R Bin, Berger A, et al. 2011. The Direct Writing of Plasmonic Gold Nanostructures by Electron-Beam-Induced Deposition. *Adv Mater*; **23**: 2657–2661.

[15] Winkler R, Schmidt F-P, Haselmann U, et al. 2017. Direct-Write 3D Nanoprinting of Plasmonic Structures. *ACS Appl Mater Interfaces*; **9**: 8233–8240.

[16] Sengupta S, Li C, Baumier C, et al. 2015. Superconducting nanowires by electron-beam-induced deposition. *Appl Phys Lett*; **106**: 042601.

[17] Córdoba R, Ibarra A, Mailly D, et al. 2018. Vertical Growth of Superconducting Crystalline Hollow Nanowires by He+ Focused Ion Beam Induced Deposition. *Nano Lett*; **18**: 1379–1386.

[18] Arnold G, Winkler R, Stermitz M, et al. 2018. Tunable 3D Nanoresonators for Gas-Sensing Applications. *Adv Funct Mater*; **28**: 1707387.

[19] Gabureac M, Bernau L, Utke I, et al. 2010. Granular Co-C nano-Hall sensors by focused-beam-induced deposition. *Nanotechnology*; **21**: 115503.

[20] Schwalb CH, Grimm C, Baranowski M, et al. 2010. A Tunable Strain Sensor Using Nanogranular Metals. *Sensors*; **10**: 9847–9856.

[21] Botman A, Mulders JJL, Hagen CW. 2009. Creating pure nanostructures from electron-beam-induced deposition using purificationtechniques: a technology perspective. *Nanotechnology*; **20**: 372001.

[22] Perez-Roldan MJ, Mulders JJL, Trompenaars F, et al. 2017. Comparison of Pd electron beam induced deposition using two precursors and an oxygen purification strategy. *Nanotechnology*; **28**: 375302.

[23] Puydinger M V, Santos D, Szkudlarek A, et al. 2018. Comparative study of post-growth annealing of Cu(hfac)2 , Co2(CO)8 and Me2Au(acac) metal precursors deposited by FEBID. *Beilstein J Nanotechnol*; **9**: 91–101.

[24] Graells S, Alcubilla R, Badenes G, et al. 2007. Growth of plasmonic gold nanostructures by electron beam induced deposition. *Appl Phys Lett*; **91**: 121112.

[25] Lewis BB, Winkler R, Sang X, et al. 2017. 3D Nanoprinting via laser-assisted electron beam induced deposition: growth kinetics, enhanced purity, and electrical resistivity. *Beilstein J Nanotechnol*; **8**: 801–812.

[26] Roberts NA, Fowlkes JD, Magel GA, et al. 2012. Enhanced material purity and resolution via synchronized laser assisted electron beam induced deposition of platinum. *Nanoscale*; **5**: 408–415.

[27] Rohdenburg M, Boeckers H, Brewer CR, et al. 2020. Efficient NH3-based process to remove chlorine from electron beam deposited ruthenium produced from (η3-c3H5)Ru(CO)3Cl. *Sci Rep*; **10**: 10901.

[28] Rohdenburg M, Winkler R, Kuhness D, et al. 2020. Water-Assisted Process for Purification of Ruthenium Nanomaterial Fabricated by Electron Beam Induced Deposition. *ACS Appl Nano Mater*; **2020**: 8352–8364.

[29] Jurczyk J, Brewer CR, Hawkins OM, et al. 2019. Focused Electron Beam-Induced Deposition and Post-Growth Purification Using the Heteroleptic Ru Complex (η3-C3H5)Ru(CO)3Br. *ACS Appl Mater Interfaces*; **11**: 28164–28171.

[30] Langford RM, Ozkaya D, Sheridan J, et al. 2004. Effects of Water Vapour on Electron and Ion Beam Deposited Platinum. *Microsc Microanal*; **10**: 1122–1123.

[31] Belić D, Shawrav MM, Gavagnin M, et al. 2015. Direct-Write Deposition and Focused-Electron-Beam-Induced Purification of Gold Nanostructures. *ACS Appl Mater Interfaces*; **7**: 2467–2479.

[32] Prashant Poddar N, Mukherjee · S K. 2019. Effect of substrates and post-deposition annealing on rf-sputtered Al-doped ZnO (AZO) thin films. *J Mater Sci Mater Electron*; **30**: 14269–14280.

[33] Carden WG, Thorman RM, Unlu I, et al. 2019. Design, Synthesis, and Evaluation of CF3AuCNR Precursors for Focused Electron Beam-Induced Deposition of Gold. *ACS Appl Mater Interfaces*; **11**: 11976–11987.

[34] Olsen VS, Bazioti C, Baldissera G, et al. 2019. Effects of Substrate and Post-Deposition Annealing on Structural and Optical Properties of (ZnO)1−x(GaN)x Films. *Phys Status Solidi Basic*

Res; **256**: 1–7.

[35] Pastor D, Cuscó R, Artús L, et al. 2006. The effect of substrate on high-temperature annealing of GaN epilayers: Si versus sapphire. *J Appl Phys*; **100**: 043508.

[36] Barth S, Huth M, Jungwirth F. 2020. Precursors for direct-write nanofabrication with electrons. *J Mater Chem C*; **8**: 15884–15919.

[37] Carden WG, Lu H, Spencer JA, et al. 2018. Mechanism-based design of precursors for focused electron beam-induced deposition. *MRS Commun*; **8**: 343–357.

[38] Zarzar LD, Swartzentruber BS, Harper JC, et al. 2012. Multiphoton Lithography of Nanocrystalline Platinum and Palladium for Site-Specific Catalysis in 3D Microenvironments. *J Am Chem Soc*; **134**: 4007–4010.

[39] Cuenya BR. 2013. Metal Nanoparticle Catalysts Beginning to Shape-up. *Acc Chem Res*; **46**: 1682–1691.

[40] Atashbar MZ, Banerji D, Singamaneni S. 2005. Room-temperature hydrogen sensor based on palladium nanowires. *IEEE Sens J*; **5**: 792–797.

[41] Ardy Nugroho FA, Robin Eklund, Sara Nilsson, et al. 2018. A fiber-optic nanoplasmonic hydrogen sensor via pattern-transfer of nanofabricated PdAu alloy nanostructures. *Nanoscale*; **10**: 20533–20539.

[42] Bhuvana T, Kulkarni GU. 2008. Highly Conducting Patterned Pd Nanowires by Direct-Write Electron Beam Lithography. *ACS Nano*; **2**: 457–462.

[43] Sharma B, Kim JS. 2017. Pd/Ag alloy as an application for hydrogen sensing. *Int J Hydrogen Energy*; **42**: 25446–25452.

[44] Rosenberg SG, Barclay M, Fairbrother DH. 2014. Electron Induced Surface Reactions of Organometallic Metal(hfac) 2 Precursors and Deposit Purification. *ACS Appl Mater Interfaces*; **6**: 8590–9601.

[45] Radha B, Kulkarni GU. 2010. Patterned Synthesis of Pd4S: Chemically Robust Electrodes and Conducting Etch Masks. *Adv Funct Mater*; **20**: 879–884.

[46] Stark TJ, Mayer TM, Griffis DP, et al. 1992. Formation of complex features using electron-beam direct-write decomposition of palladium acetate. *J Vac Sci Technol B Microelectron Nanom Struct*; **10**: 2685–2689.

[47] Reetz MT, Winter M, Dumpich G, et al. 1997. Fabrication of Metallic and Bimetallic Nanostructures by Electron Beam Induced Metallization of Surfactant Stabilized Pd and Pd/Pt Clusters. *J Am Chem Soc*; **119**: 4539–4540.

[48] Stark TJ, Mayer TM, Griffis DP, et al. 1991. Electron beam induced metalization of palladium acetate. *J Vac Sci Technol B Microelectron Nanom Struct*; **9**: 3475–3478.

[49] Gross ME, Brown WL, Harriott LR, et al. 1989. Ion-beam direct-write mechanisms in palladium acetate films. *J Appl Phys*; **66**: 1403–1410.

[50] Gross ME, Appelbaum A, Gallagher PK. 1987. Laser direct-write metallization in thin palladium acetate films. *J Appl Phys*; **61**: 1628–1632.

[51] Harriott LR, Cummings KD, Gross ME, et al. 1986. Decomposition of palladium acetate films with a microfocused ion beam. *Appl Phys Lett*; **49**: 1661–1662.

[52] Matula RA. 1979. Electrical resistivity of copper, gold, palladium, and silver. *J Phys Chem Ref Data*; **8**: 1147–1298.

[53] Tomotoshi D, Oogami R, Kawasaki H. 2021. Highly Conductive, Flexible, and Oxidation-Resistant Cu-Ni Electrodes Produced from Hybrid Inks at Low Temperatures. *ACS Appl Mater Interfaces*; 10.1021/acsami.1c04235.

[54] Hwan Park J, Eol Lee H, Kyu Jeong C, et al. 2019. Self-powered flexible electronics beyond thermal limits. *Nano Energy*; **56**: 531–546.

[55] Lu QH, Zheng F. 2018. Polyimides for electronic applications. In: *Advanced Polyimide Materials: Synthesis, Characterization, and Applications*. Elsevier, pp. 195–255.

[56] Simon B, Bouyer C, De Sio S, et al. 2018. Characterization of palladium species after γ-irradiation of a TBP–alkane–Pd(NO3)2 system. *RSC Adv*; **8**: 21513–21527.

[57] Karakanov EA, Zolotukhina A V., Ivanov AO, et al. 2019. Dendrimer-Encapsulated Pd Nanoparticles, Immobilized in Silica Pores, as Catalysts for Selective Hydrogenation of Unsaturated Compounds. *ChemistryOpen*; **8**: 358–381.

[58] Hasik M, Bernasik A, Drelinkiewicz A, et al. 2002. XPS studies of nitrogen-containing conjugated polymers–palladium systems. *Surf Sci*; **507**–**510**: 916–921.

[59] Winkler K, Noworyta K, De Bettencourt-Dias A, et al. 2003. Structure and properties of C60-Pd films formed by electroreduction of C60 and palladium(II) acetate trimer: Evidence for the presence of palladium nanoparticles. *J Mater Chem*; **13**: 518–525.

[60] Bilgilisoy E, Thorman RM, Barclay MS, et al. 2021. Low Energy Electron- and Ion-Induced Surface Reactions of Fe(CO) 5 Thin Films . *J Phys Chem C*; **125**: 17749–17760.

[61] Fernández-Pacheco A, De Teresa JM, Córdoba R, et al. 2009. Metal-insulator transition in Pt-C nanowires grown by focused-ion-beam- induced deposition. *Phys Rev B - Condens Matter Mater Phys*; **79**: 1–12.

[62] Bhuvana T, Gregoratti L, Heun S, et al. 2009. Electron resist behavior of Pd hexadecanethiolate examined using x-ray photoelectron spectroscopy with nanometric lateral resolution. *Langmuir*; **25**: 1259–1264.

[63] Epping A, Volk C, Buckstegge F, et al. 2019. Insulating State in Low-Disorder Graphene Nanoribbons. *Phys Status Solidi B*; **256**: 1900269.

[64] Thøgersen A, Mayandi J, Vines L, et al. 2011.

Composition and structure of Pd nanoclusters in SiOx thin film. *J Appl Phys*; **109**: 084329.

[65] Porrati F, Sachser R, Schwalb CH, et al. 2011. Tuning the electrical conductivity of Pt-containing granular metals by postgrowth electron irradiation. *J Appl Phys*; **109**: 063715.

[66] Plank H, Noh JH, Fowlkes JD, et al. 2014. Electron-Beam-Assisted Oxygen Purification at Low Temperatures for Electron-Beam-Induced Pt Deposits: Towards Pure and High-Fidelity Nanostructures. *ACS Appl Mater Interfaces*; **6**: 1018–1024.

[67] Fong Y-Y, Visser BR, Gascooke JR, et al. 2011. Photoreduction Kinetics of Sodium Tetrachloroaurate under Synchrotron Soft X-ray Exposure. *Langmuir*; **27**: 8099–8104.